https://doi.org/10.5194/egusphere-2023-2605
Preprint. Discussion started: 21 December 2023

Toward Long-Term Monitoring of Regional Permafrost Thaw with Satellite InSAR

Taha Sadeghi Chorsi[1], Franz J. Meyer[2], and Timothy H. Dixon[1]

[1]School of Geosciences, University of South Florida, Tampa, FL, USA
[2]Geophysical Institute, University of Alaska Fairbanks, AK, USA

Correspondence: Taha Sadeghi Chorsi (taha4@usf.edu)

Abstract. We estimate active layer thickness (ALT) for part of northern Alaska's permafrost zone for summer 2017 to 2022 using satellite data from Sentinel-1 and ICESat-2. Interferograms were inverted using a Short Baseline Subset (SBAS) approach to estimate the amplitude of seasonal subsidence. ALT was estimated from the measured subsidence. ICESat-2 products were used to validate the InSAR displacement time-series. Most subsidence occurs between June and August in our study area. The maximum amplitude of seasonal subsidence was 2-6 cm, with ALT exceeding 1.5 m. Estimated ALT is in good agreement with in-situ and other remotely sensed data, but is sensitive to assumed thaw season onset, indicating the need for reliable surface temperature data. Our results suggest the feasibility of long-term permafrost monitoring with satellite InSAR.

1 Introduction

Permafrost is usually covered with soil or sediment – the active layer – which freezes and thaws seasonally. This layer also moderates the impacts of surface temperature changes (Dobinski, 2011). The annual freeze-thaw cycle of the active layer causes significant surface height change due to the volume difference between ice and liquid water. Active layer thickness (ALT) can be estimated using simplified physical models and surface subsidence measurements during the thaw season (Liu et al., 2012, 2014, 2015; Schaefer et al., 2015; Hu et al., 2018). ALT is expected to increase as Arctic temperatures rise and permafrost undergoes long-term thaw, so remote monitoring of this feature is important.

In the last three decades satellite-based Interferometric Synthetic Aperture Radar (InSAR) has been used to monitor a variety of Earth processes that generate subtle surface displacements, including earthquake and volcano deformation, and reservoir compaction from fluid withdrawal (e.g., Bürgmann et al., 2000). Recent examples include earthquake after-slip (e.g., Sadeghi Chorsi et al., 2022b, a), volcano deformation (e.g., Poland and Zebker, 2022; Grapenthin et al., 2022), groundwater extraction (e.g., Castellazzi et al., 2016), carbon sequestration (e.g., Yang et al., 2015; Vasco et al., 2020), seismicity induced by fluid injection (e.g., Deng et al., 2020), coastal sea ice dynamics (e.g., Dammann et al., 2019) and coastal flood hazard (e.g., Bekaert et al., 2017; Zhang et al., 2022). Pioneering work by L. Liu (Liu et al., 2010, 2012) demonstrated the utility of InSAR to monitor long-term permafrost thaw and changes in ALT. Here, we use InSAR from the Sentinel-1 satellite constellation to investigate permafrost thaw on the North Slope of Alaska for the period 2017 to 2022, focusing on multi-year changes in ALT.

https://doi.org/10.5194/egusphere-2023-2605
Preprint. Discussion started: 21 December 2023

2 Previous Work

Satellite remote sensing of permafrost has been ongoing for at least three decades (e.g., Peddle and Franklin, 1993). In terms of microwave studies, Singhroy et al. (2007) used RADARSAT-1 to monitor permafrost activity and landslide motion around the Mackenzie Valley Pipeline Corridor, Canada. Rykhus and Lu (2008) used JERS-1 L-band data to detect thaw settlement over the Alaskan Arctic coastal plain. Liu et al. (2010) used ERS-1 and -2 SAR images to monitor permafrost on the North slope of Alaska, observing seasonal subsidence of $\sim$1-4 cm and average secular subsidence of $\sim$1-4 $\mathrm{cm/decade}$. Liu et al. (2012) used SAR data to develop a novel ALT retrieval model, relating InSAR-derived subsidence to ALT using air temperature, soil texture, and organic matter thickness, assuming subsidence in a given thaw season is related to the volume reduction associated with the phase change between ice and water. We follow a similar approach in this study. Schaefer et al. (2015) used ALOS PALSAR data from 2006-2010 to estimate average ALT and long-term subsidence in Barrow, Alaska. Their model showed a good agreement between remotely estimated ALT, Ground Penetrating Radar (GPR) and in-situ data for more than 75% of the area. Daout et al. (2017) used multi-temporal InSAR observations to quantify ALT over Northwestern Tibet. They found that unconsolidated sediments in flat basins have higher seasonal subsidence amplitude compared to slope sediments and proposed that ground water was the key controlling factor. Iwahana et al. (2016) used InSAR data from ALOS PALSAR together with GPS data to study the long-term impacts of wildfire on the permafrost regime in the Anaktuvuk, Alaskan North Slope. Chen et al. (2018) used Sentinel-1 InSAR data to estimate seasonal thaw subsidence and inter-annual elevation change from 2016 to 2017 in Yedoma, Russia. They found that the top of the flat Yedoma upland exhibits large seasonal subsidence, and suggested that the delayed thaw season in 2017 was related to air temperature fluctuations. Strozzi et al. (2018) used Sentinel-1 InSAR to measure seasonal thaw subsidence in four sites, observing seasonal subsidence from 2 to 10 cm. Liu and Larson (2018) used GPS interferometric reflectometry (GPS-IR) at Barrow, Alaska, showing that surface elevation could be measured reliably during snow-free days. Hu et al. (2018) also used GPS-IR here, observing elevation changes with a seasonal amplitude of 5 cm. Michaelides et al. (2019) used ALOS data to estimate seasonal subsidence, long-term subsidence and ALT to develop a fire response model. Bartsch et al. (2019) used Sentinel-1 (C-band) and COSMO-Skymed (X-band) SAR images between 2013 to 2018 to monitor seasonal subsidence in central Yamal, Russia. Wang et al. (2020) used Sentinel-1 time-series in northern Canada, demonstrating the utility of C-band radar for monitoring ALT in a sub-arctic tundra region. Chen et al. (2020) used ALOS PALSAR data to monitor ALT in Toolik, Alaska. Honglei et al. (2021) used ALOS PALSAR for the period 2007 to 2010 to permafrost-related subsidence in the Qinghai-Tibet Plateau, observing settlement up to 12 cm. Michaelides et al. (2021) and Chen et al. (2023) used L-band UAVSAR InSAR and AirMOSS P-band polarimetric backscatter data over different sites in Alaska and western Canada to simultaneously estimate seasonal subsidence, ALT and volumetric water content. Here, we use Sentinel-1 interferometry to monitor seasonal subsidence and ALT changes from 2017 to 2022 for part of northern Alaska.

3 Study Area

Our main study area is located in northern Alaska in the vicinity of the Sag river and Dalton highway (69.68 N, 148.7 W; Figure-1). It is $\sim$50 km south of Prudhoe Bay and $\sim$130 km west of the Brookes range. It is located in a continuous permafrost

https://doi.org/10.5194/egusphere-2023-2605
Preprint. Discussion started: 21 December 2023

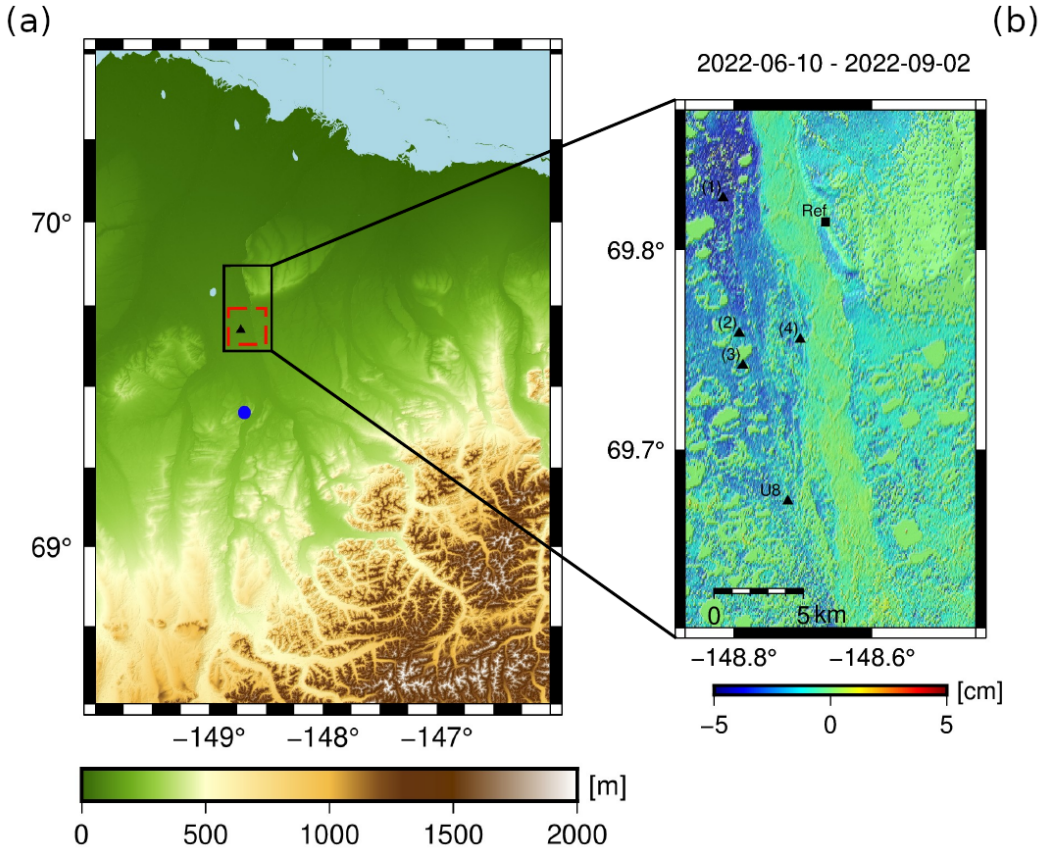

Figure 1. (a): DEM of study area in northern Alaska. Solid black box is expanded in Figure-1b, red box outlines Figure-5. Triangle shows CALM site (U8) used to compare ALT. Blue circle represents location of closest meteorological site used in this study (Sagwon). (b): LOS displacement from 2022-06-10 to 2022-09-02. Negative values means displacement away from satellite. DEM relief map is shown in background. Triangles show location of displacement time-series shown in Figure-3 and CALM site. Black square represents reference point for InSAR used in this study.

region with more than 90% permafrost coverage (Jorgenson et al., 2008). The site is described as having 23 cm organic layer thickness with seasonal high water table subject to saturation. The U8 CALM site's vegetation coverage is classified as graminoid-moss tundra, graminoid, prostrate-dwarf-shrub, and moss tundra (https://www2.gwu.edu/~calm/data/webforms/u8_f.htm). The Circumpolar Arctic Vegetation Map (CAVM) describe graminoid and prostrate-dwarf-shrub vegetation as 5-10 cm tall (CAVM Team, 2003). This short vegetation is likely favorable for shorter radar wavelength radars like Sentinel-1's C-band (wavelength ∼5.5 cm) to retain phase coherence. For comparison we also studied the Beta site of the APEX (Alaska Peatland EXperiment), located approximately 30 km southwest of Fairbanks (64.696 N, 148.322 W). This site is located in discontinuous permafrost zone with abundant black spruce, up to 5 m in height.

https://doi.org/10.5194/egusphere-2023-2605
Preprint. Discussion started: 21 December 2023

4 Methods

4.1 InSAR Data Processing

4.1.1 Data and Material

Sentinel-1 SAR images from June to September 2017 to 2022 were selected to cover the end of freeze season to the end of thaw season (Table-S1). Changes in surface scattering characteristics in the freeze season (surface covered with snow and ice) could decorrelate the radar wave. We used the Alaska Satellite Facility's Hybrid Pluggable Processing Pipeline (HyP3) software to form interferograms (Hogenson et al., 2020). HyP3 uses the Copernicus GLO-30 Digital Elevation Model (DEM) for scene coregistration and topographic phase corrections (ESA, 2021). Interferograms were filtered using the adaptive phase filter in Goldstein and Werner (1998). Individual interferograms were unwrapped using a minimum-cost-flow algorithm (Chen and Zebker, 2002) and geocoded to a 30 m grid spacing. We used the open-source Miami InSAR time-series software in python (MintPy) to generate LOS displacement time-series from the unwrapped and geocoded interferograms (Fattahi et al., 2016; Yunjun et al., 2019). Geocoded LOS displacement data for active layer thickness estimation was then extracted for the study area.

4.1.2 Reference Point Selection

InSAR is a double-difference technique that measures phase differences between SAR observations in space and time. To relate these phase difference measurements to surface displacement, we need to choose a reference location with assumed or known displacement. In permafrost regions, rock outcrops are a suitable reference locations as they can be assumed to show only minimal displacement, but may not be available for all regions. For this study, we use two criteria for reference point selection: first, we require the point to have high temporal coherence (> 0.8) to avoid introducing noise into our time series. Second, we look for locations that either are rock outcrops or lie in a floodplain (but not a river channel, which can undergo large elevation changes from erosion/deposition events; see Figure-S1). Liu et al. (2010) point out that floodplains usually have well-drained sandy soils and hence tend not to experience significant frost heave. Figure-1b shows the reference point we identified using these criteria, a rock outcrop immediately northeast of our study area which remains coherent (temporal coherence $\sim$0.95) during the 2017 to 2022 thawing seasons.

4.1.3 Atmospheric delay correction

Atmospheric effects are one of the main error sources in the InSAR process (Meyer et al., 2006). While InSAR data can be affected by both the ionosphere and the troposphere, here we focus on tropospheric effects as ionospheric impacts are less pronounced in C-band data (Meyer, 2011). Tropospheric phase impacts can be modeled as (Ding et al., 2008):

$$\Delta\phi = \phi_2 - \phi_1 = \frac{4\pi}{\lambda}[d_2 - d_1] + \frac{4\pi}{\lambda}[\delta d_2 - \delta d_1] \quad (1)$$

https://doi.org/10.5194/egusphere-2023-2605
Preprint. Discussion started: 21 December 2023

where ϕ is the phase of a SAR image, d is the range from satellite to surface, δd is the tropospheric propagation delay, and λ is the radar wavelength. Tropospheric phase signals in InSAR data can be caused by two processes: changes in the atmospheric stratification and turbulent mixing. The stratified phase component typically correlates with topography (Hanssen, 2001) and may be estimated based on delay-elevation correlations, then removed from the radar phase (Doin et al., 2009). The turbulent component plays an important role in phase delay because it is uncorrelated in time and space, although its amplitude is much less than the stratified component. According to (1) if the atmospheric propagation conditions at the time of SAR acquisitions are not the same (δd_2- $\delta d_1 \neq 0$), then tropospheric phase components will be introduced, contaminating the true displacement signal. To reduce these tropospheric effects, one approach is to apply a global weather model. This approach mainly reduces the stratified component. We applied the atmospheric correction model described in Jolivet et al. (2011, 2014) using ECMWF reanalysis (ERA-5) datasets (Hersbach et al., 2020).

4.2 ICESat-2 data processing

We used the ICESat-2 level 3A product for land and vegetation height (ATL-08) to validate the InSAR time-series displacement estimates. While the nominal temporal resolution of ICESat-2 data is 91 days, cloud cover greatly limits the amount of usable data in Alaska (e.g., Neuenschwander and Pitts, 2019). Two observations were available in our study area, acquired on 2021-06-08 and 2021-09-06. We used the "h_te_best_fit" parameter, which estimates terrain height by fitting a plane to along-track points in each 100 m segment and report the height of the middle of the fitted plane (Neuenschwander and Magruder, 2019; Neuenschwander et al., 2021). Due to pointing-related errors, observations are not always repeated in expected locations, which amplifies the height uncertainty. To address this issue, we divided the study area into 50 m grid cells, and assigned each observation in 2021-06-08 and 2021-09-06 to one of those grid cells. Figure-S1 shows the height difference between all reported observations in the study area between 2021-06-08 and 2021-09-06. In the limited area where both InSAR and ICESat-2 data are available (four points shown in Figure-1a), we used the ICESat-2 data to evaluate the InSAR results (Figure-3).

4.3 ALT estimation model

To relate the InSAR observations to ALT, we assume that the measured LOS displacements are predominantly due to vertical motion (negligible horizontal motion) and this vertical motion is caused by thawing ground ice in the active layer. The assumption of negligible horizontal motion is justified because the data time interval is short and the technique does not sense long-term tectonic motion. We observed large displacements in August 2018, $\sim$130 km east of study area due to the M 6.4 earthquake (USGS hypocenter at north of Brooke range: 145.291 W, 69.576 N, depth 15.8 km). Since our study area was far from this area, we believe most of the deformation in thaw season is because of ground ice thawing. We project the LOS displacements into the vertical direction using the local incidence angle (θ) for each radar pixel (see Equation-3). We follow the simplified Stefan solution to estimate depth of thawing in the soil (Nelson et al., 1997) aided by field-observed air temperature data. We also assume that subsidence can be related to a simple thaw index, for example the accumulated degree days of thawing (ADDT).

https://doi.org/10.5194/egusphere-2023-2605
Preprint. Discussion started: 21 December 2023

4.3.1 ADDT calculation

To calculate ADDT, we use the NOAA Climate Data Online (CDO) tool to find nearby meteorological stations. The closest station is ∼20 km south to our study area (Name: Sagwon, Figure-1a). We assume that our study area has the same temperature trend as this station from 2017 to 2022. We define the first and last day with temperature > 0 °C as the first and last day of the thaw season. ADDT is defined by the following equation (Riseborough, 2003):

$$ADDT = \int_0^{\alpha_s} (T_s - T_f)dt \approx \sum_0^{\alpha_s} \bar{T_s} \tag{2}$$

where α_s is the duration of thawing season, in days. T_s is surface temperature (°C), T_f is equal to freezing point, 0 °C, and $\bar{T_s}$ is daily mean surface temperature. Due to lack of in-situ surface temperature data, we set $\bar{T_s}$ using air temperature observations.

4.3.2 Seasonal Amplitude Inversion

The relationship between the seasonal vertical surface displacement magnitude and ADDT can be written as (Liu et al., 2012; Schaefer et al., 2015):

$$D_i = \frac{LOS}{\cos(\theta)} = E(\sqrt{A_{2,i}} - \sqrt{A_{1,i}}) + \varepsilon \tag{3}$$

where D_i is the vertical displacement estimate for a given pixel in the i^{th} interferogram, θ is the local incidence angle at that pixel calculated from nadir, E is the amplitude of the seasonal vertical displacement estimate which reflects physical parameters such as soil thermal conductivity, latent heat of fusion, soil density and relative water content. $A_{1,i}$ and $A_{2,i}$ are normalized accumulated degree days of thawing at the first and second acquisition date. ε is an error term that captures model deficiencies, noise, and other unknown error sources. We do not consider secular (long-term) displacement signals in (3) because we analyze the thaw seasons of 2017 to 2022, separately. We can rewrite (3) in matrix form considering the interferograms listed in table-S1, to estimate E using least squares.

$$\begin{bmatrix} D_1 \\ D_2 \\ \vdots \\ D_N \end{bmatrix} = \begin{bmatrix} \sqrt{A_{2,1}} - \sqrt{A_{1,1}} \\ \sqrt{A_{2,2}} - \sqrt{A_{1,2}} \\ \vdots \\ \sqrt{A_{2,N}} - \sqrt{A_{1,N}} \end{bmatrix} \begin{bmatrix} E \end{bmatrix} \tag{4}$$

4.3.3 ALT Inversion

If we assume that the seasonal vertical surface displacement amplitude E is caused only by thawing ice and corresponding volume reduction, we can write E as a function of physical properties such as soil porosity, soil moisture fraction, and density of ice and water through a vertical profile from surface to depth of the active layer (Liu et al., 2012; Schaefer et al., 2015):

https://doi.org/10.5194/egusphere-2023-2605
Preprint. Discussion started: 21 December 2023

$$E = \frac{\rho_w - \rho_i}{\rho_i} \int_0^{ALT} P(z)S(z)dz \tag{5}$$

The variables ρ_w and ρ_i in (5) are the density of water and ice [$\mathrm{kg\,m^{-3}}$], respectively. $P(z)$ is the soil porosity which is a function of depth and depends on soil content. $S(z)$ is the soil moisture fraction of saturation. Here, we assume that $S(z) = 1$, which means that the active layer is fully saturated and does not change with depth (Schaefer et al., 2015). In the next section, we describe relation between porosity in depth and ALT in (5).

4.3.4 Porosity Model

We assume the soil in the active layer consists of organic matter and mineral soil. In this case, the porosity decreases exponentially with depth due to decreasing organic matter. There is one active Circumpolar Active Layer Monitoring (CALM) site inside our study area: U8 (Figure 1a). This site is described as having 23 cm organic layer thickness, consisting mainly of peat plus sand and gravel (https://www2.gwu.edu/~calm/data/webforms/u8_f.htm). We consider this organic matter thickness in modeling of porosity versus depth. We applied the formulation introduced by Liu et al. (2012) and presume that $P(z)$ is the weighted average of organic and mineral matter:

$$P = f_{org}P_{org} + (1 - f_{org})P_{min} \tag{6}$$

where P is the porosity, and f_{org} is defined as the organic soil fraction by Schaefer et al. (2009) as:

$$f_{org} = \frac{M_{org}}{M_{org\_max}} = \frac{\rho_{org}}{\rho_{org\_max}} \tag{7}$$

In (7), M_{org} and ρ_{org} are the simulated mass of organic matter and organic soil density in a given layer of soil, respectively. M_{org_max} and ρ_{org_max} are bulk organic matter mass and bulk density for pure organic soil, respectively. We set $P_{org} = 0.95$ based on model from Bakian-Dogaheh et al. (2022). The porosity of mineral soil depends on the sand fraction of soil. To estimate mineral porosity, P_{min}, we utilized the porosity-sand fraction relation provided in Liu et al. (2012):

$$P_{min} = 0.489 - 0.00126\, fr_{sand} \tag{8}$$

We used Global Land Data Assimilation System (GLDAS) soil parameters with 0.25° spatial resolution to extract fr_{sand}, the soil sand fraction (Rodell et al., 2004). We set $P_{min} = 0.488$, and $\rho_{org\_max} = 130$ [$\mathrm{kg\,m^{-3}}$] for bulk density of peat (Grigal et al., 1989; Hossain et al., 2015). As mentioned earlier, to formalize with depth, we assume the organic matter amount decreases exponentially with depth:

$$\rho_{org} = B\exp(-kz) \tag{9}$$

https://doi.org/10.5194/egusphere-2023-2605
Preprint. Discussion started: 21 December 2023

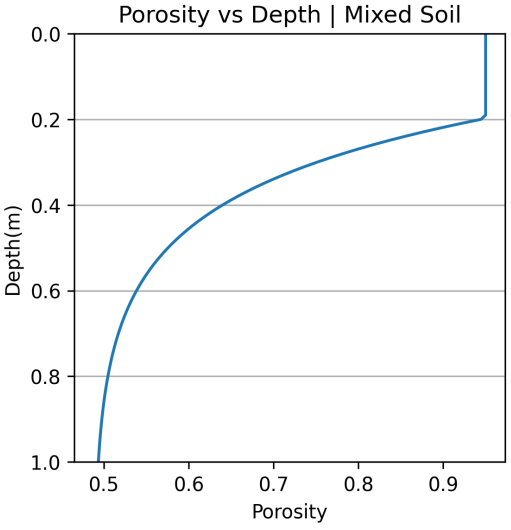

Figure 2. Depth-porosity model used in this study assuming a mixture of organic and mineral matter.

where k is an empirical constant [m^{-1}], set to 5.5 (Liu et al., 2012; Jackson et al., 2003). To retrieve B, we use simulated mass of organic matter (M_{org}: total soil carbon content) from Johnson et al. (2011) and Mishra and Riley (2012) and ensure that total carbon mass is conserved:

$$\int_0^{root} B \exp(-kz)\, dz = M_{org} \tag{10}$$

The spatial divergence of total soil carbon content for the 0-100 cm depth range is large in Arctic tundra regions considering vegetation type. Johnson et al. (2011) and Mishra and Riley (2012) estimated M_{org} around our study area at [60-80] and [50-70] [$\mathrm{kg\,m}^{-2}$], respectively. We set $M_{org} = 70$ [$\mathrm{kg\,m}^{-2}$]. Root depth is the maximum observed ALT at a given site since roots cannot penetrate solid ice. Here, we set maximum root depth at 1.1 m because maximum observed ALT at site U8 is reported as $\sim$1.1 m for 2022. Then we solve (10) for B and replace it in (9). Figure-2 shows the relation between porosity and depth in a mixed soil. We set $P = 0.95$ for the first $\sim$20 cm depth reflecting organic matter thickness. After 20 cm depth, the porosity decreases exponentially, reaching its minimum near the top of the frost table.

Finally, we put all equations into (5) and use a numerical bisection algorithm to solve for upper integral limit, ALT. We set the accuracy of bisection to be at the mm level.

https://doi.org/10.5194/egusphere-2023-2605
Preprint. Discussion started: 21 December 2023

5 Results and Discussion

5.1 Validation of InSAR Surface Displacement Estimates

We used ICESat-2 ATL-08 products to evaluate our InSAR time-series results. We found four locations in common between ICESat-2 and InSAR data for the 2021 thaw season, primarily limited by cloud cover (Figure-S1). Unfortunately, there were no suitable ICESat-2 comparison data for 2019, 2020 and 2022 thaw season. ATL-08 reports surface height relative to the WGS84 datum since mid-2018. To compare with relative InSAR data, we subtracted the two available ICESat-2 height data and assign the first date's height as zero elevation. This is a reasonable assumption because the two datasets have comparable start dates, June 8 for ICESat-2, and June 3 for SAR. Figure-3 shows that with these assumptions, the two approaches agree well. This indicates that our reference point experiences negligible change during the study period. Reference point selection for InSAR is difficult in permafrost regions as most area subside during thaw season. Comparing InSAR displacement with reliable and available ICESat-2 data could be an option to evaluate result in remote areas. However, finding suitable repeated ICESat-2 points is also difficult because of LiDAR pointing errors, cloud cover, and vegetation canopy density. The chosen locations for comparison here are less than 50 m distant (grid cell size) and have less than 7% slope difference.

https://doi.org/10.5194/egusphere-2023-2605
Preprint. Discussion started: 21 December 2023

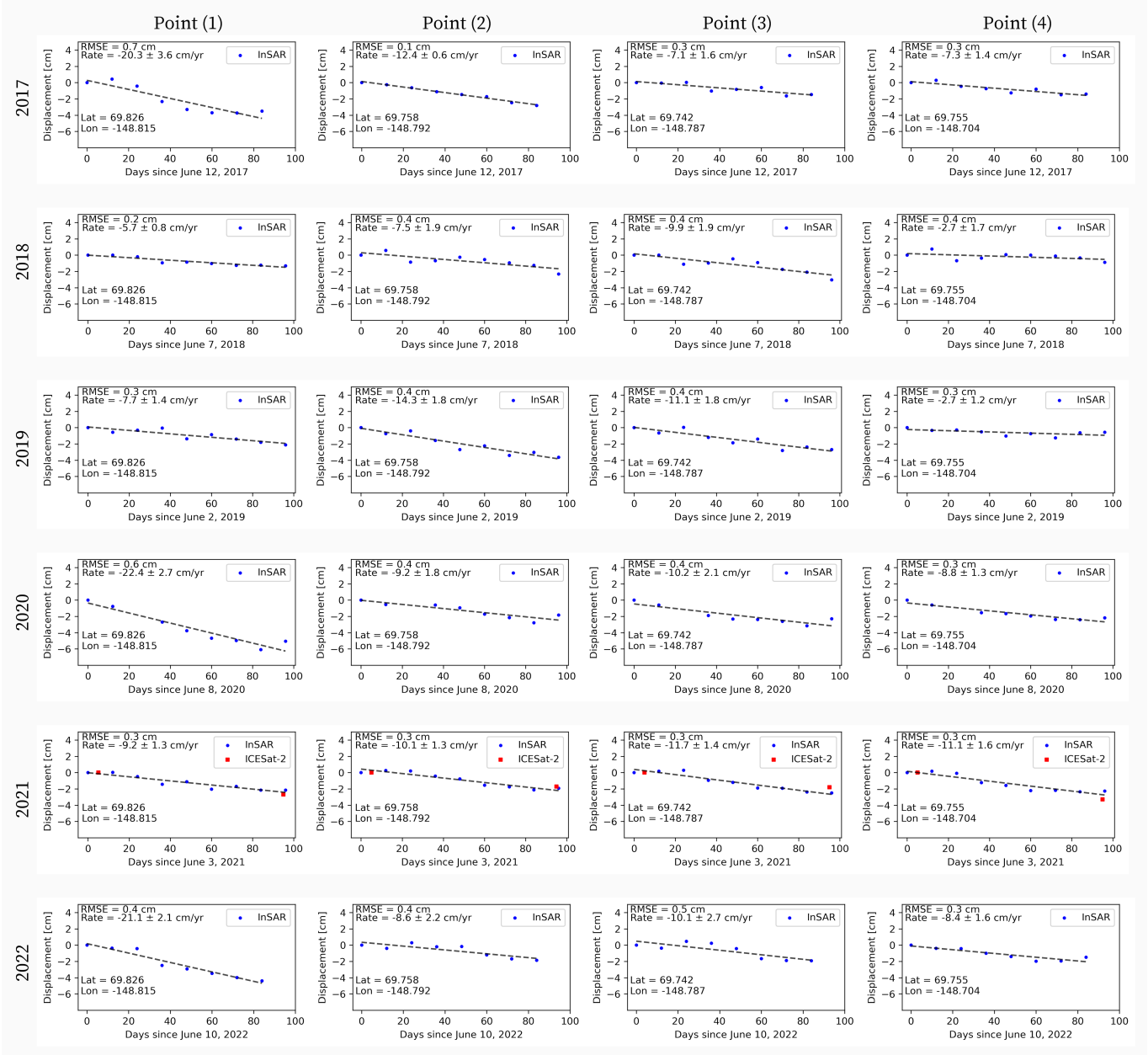

Figure 3. LOS displacement time-series for four locations (black triangles in Figure-1b) with respect to the first SAR acquisition in the thaw season. Black dashed lines are best-fitting regression lines for InSAR LOS displacement only. Rate and RMSE of fitted lines are shown in the top-left of each sub-figure. Red squares in 2021 show ICESat-2 ATL-08 terrain height product. Latitude and longitude of each analyzed location are shown in the bottom-left of each panel.

https://doi.org/10.5194/egusphere-2023-2605
Preprint. Discussion started: 21 December 2023

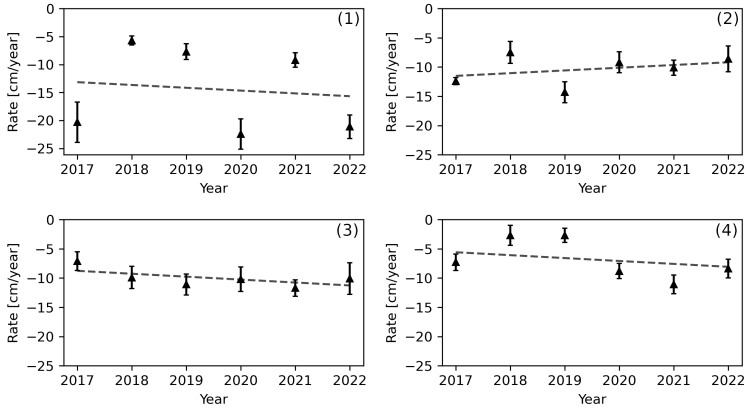

Figure 4. Rate comparison of LOS displacement between selected points shown in Figure-1b. Rate and an error bar are from fitted linear line (See Figure-3).

5.2 Estimated Seasonal Vertical Displacement and ALT

Figure-3 shows time-series for the four locations shown in Figure-1b. The maximum amplitude of subsidence for these locations ranges from 2-6 cm. Location (4) and location (1) have the minimum and maximum subsidence amplitude in the entire time-series. Most subsidence occurs in the first two months of data acquisition (Mid-June to mid-August) for all locations. The subsidence amplitude is similar between the four locations (up to $\sim$2 cm) in 2021. The maximum rate of subsidence is $\sim$20 $\mathrm{cm/year}$ and the rate is approximately linear for most locations, with a root mean square error (RMSE) of the linear trend of less than 1 cm for all four locations from 2017 to 2022. Figure-4 shows the subsidence rate change at the four locations over six years. No clear long-term trend is observed. Location (1) has the largest rate variation, from 5.7 in 2018 to 22.4 $\mathrm{cm/year}$ in 2020. Location (3) has the minimum rate variation, 7.1 in 2017 to 11.7 $\mathrm{cm/year}$ in 2021. We do not observe correlation between subsidence rates at the various locations. For example, location (1) shows the fastest subsidence, with high rates in 2017, 2020 and 2022 but much smaller rates in 2018, 2019 and 2021. Location (2)'s fastest subsidence occurs in 2019 while the fastest rates for point-3 and 4 occurred in 2019 and 2021.

Figure-5 shows the seasonal vertical displacement amplitude and its RMSE calculated from (4) and estimated ALT from 2017 to 2022 (red box in Figure-1a). The shallowest overall ALT in this area occurred in 2018 and 2021. The deepest ALT occurred in 2019 and 2020. The variation in these estimates may in part reflect uncertainty in thaw season length. Thaw season usually starts around May 20 and ends around September 20, but the accumulated degree days differ each year. Sagwon station data for this time period shows that the maximum and minimum ADDT occurred in 2019 and 2018, respectively.

https://doi.org/10.5194/egusphere-2023-2605
Preprint. Discussion started: 21 December 2023

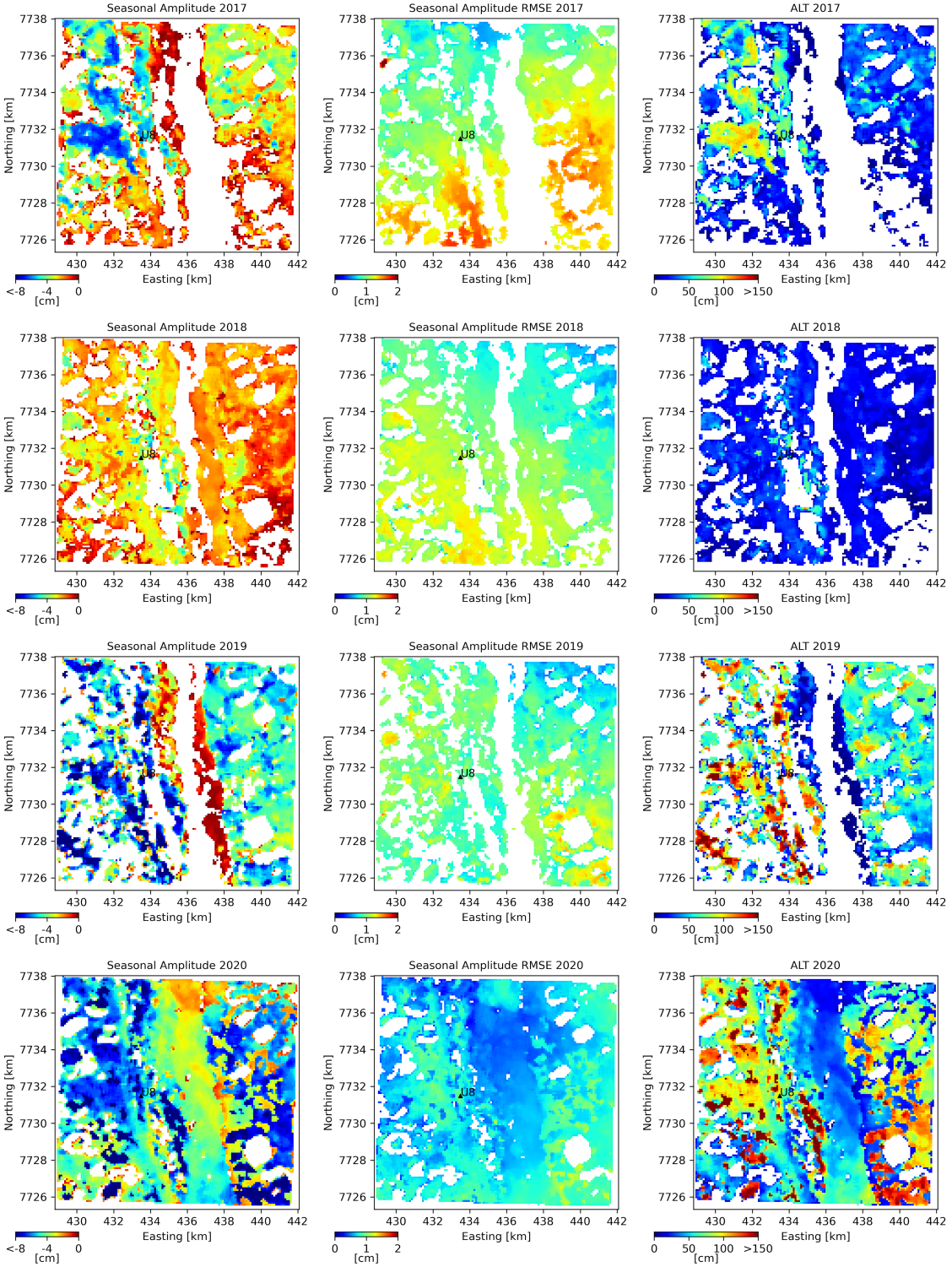

Figure 5. Estimated seasonal amplitude, its RMSE and ALT for study area (red box Figure-1a) from 2017 to 2022. Black triangle shows location of CALM site U8. White areas represent low coherence which are masked out in the model calculations. The Sag river runs south to north in the center of each panel (See Figure-S1).

https://doi.org/10.5194/egusphere-2023-2605
Preprint. Discussion started: 21 December 2023

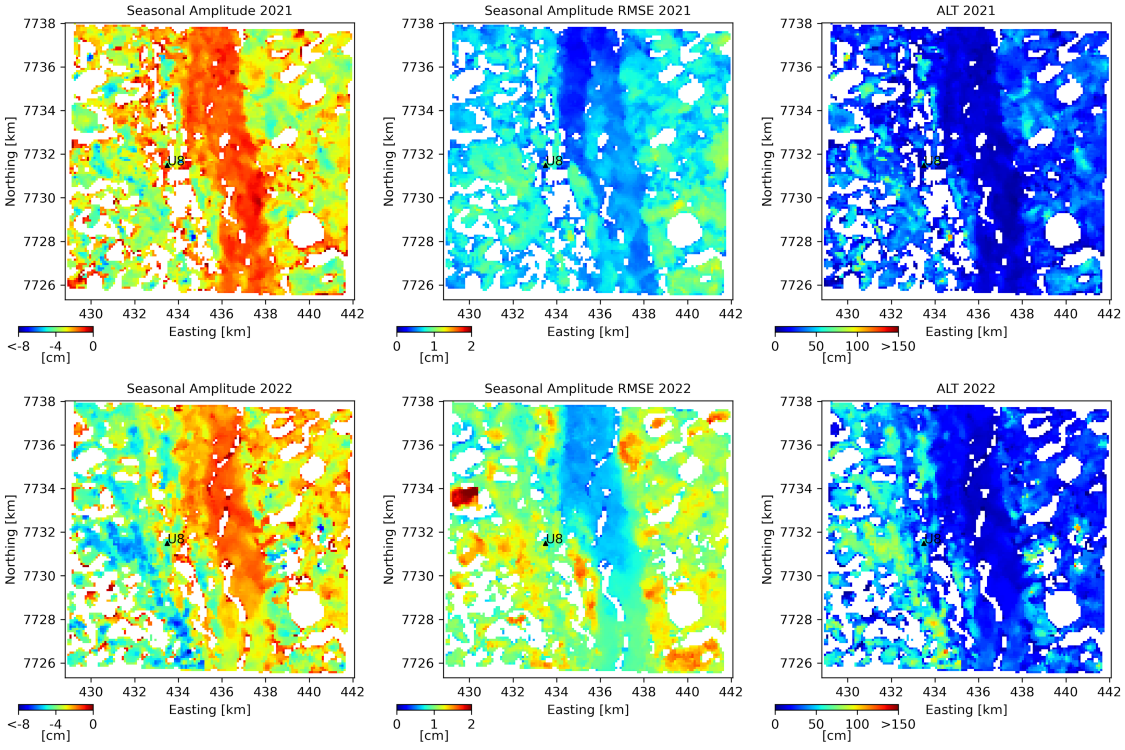

Figure 5. Continued

5.3 ALT Evaluation

We can compare our results with in-situ data. CALM site U8 is a one hectare area with 121 sample square arrays. Each array has a $\sim$10 m length. Its ALT has been observed at the end of the thaw season since 1996. Thaw depth is measured by pushing a metal rod into the soil to refusal, assumed to represent the top of the permanently frozen layer. The ALT is not reported when the array intersects large ponds or rocks. The mean of 121 ALT measurements and their RMSE are reported. Our approach for reporting the InSAR-derived ALT is similar. We averaged ALT pixels with the center of closest pixel to U8, a radius of 100 m, and calculated the corresponding RMSE (Table-1).

Figure 6 shows ALT data around the U8 CALM site for different years. Our estimated ALT agrees within uncertainty with in-situ data in five of the years, 2017, 2018, 2019, 2021 and 2022 (Table-1). In-situ ALT is not reported for 2020.

Chen et al. (2023) estimated ALT and volumetric water content for large areas in Alaska covering the U8 CALM site using L-band UAVSAR and AirMOSS P-band polarimetric SAR, respectively. Their result is in reasonable agreement with in-situ data and this study considering joint uncertainties. Data processing details are provided in Michaelides et al. (2021) and Chen et al. (2023). Table-1 shows a summary of the ALT comparison.

https://doi.org/10.5194/egusphere-2023-2605
Preprint. Discussion started: 21 December 2023

Table 1. Estimates of ALT at CALM site U8. 'ND' means no data available.

Year	This Study	CALM (U8)	Chen et al. (2022)
2017	60.9 ± 33.5	68.9 ± 11.7	49 ± 17
2018	70.7 ± 41.5	61.7 ± 11.7	ND
2019	73.7 ± 31.7	70.3 ± 12.1	ND
2020	98.5 ± 8.5	ND	ND
2021	76.7 ± 18.9	60.8 ± 9.7	ND
2022	58.7 ± 22.4	65 ± 12.1	ND

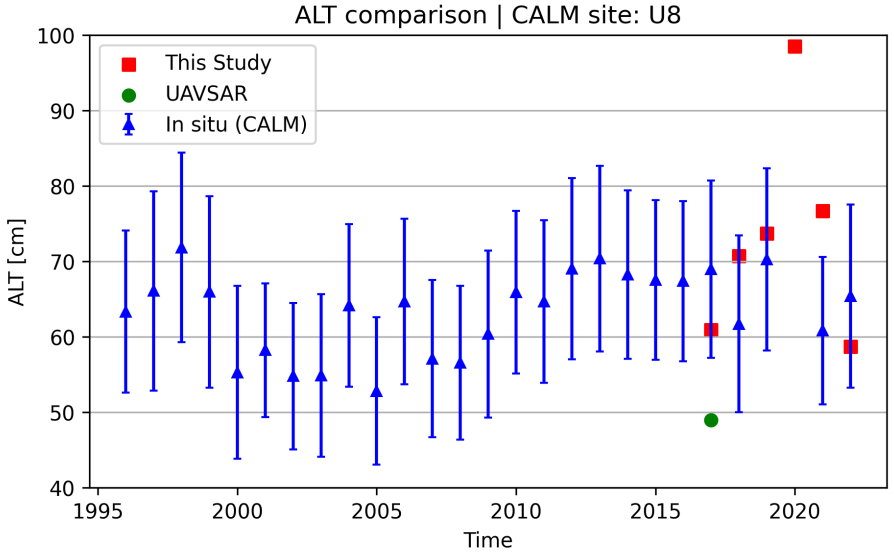

Figure 6. ALT comparison at CALM site U8. Blue triangles represent average in-situ ALT from manual mechanical probing across all grid cell from 1996 to 2022 (https://www2.gwu.edu/ calm/data/north.htm). Green circle is estimated ALT for the closest pixel to U8, using airborne L- and P-band SAR images (Chen et al., 2022). Red squares (this study) are average estimated ALT for pixels with 100 m distance to U8. In-situ ALT is not reported for 2020.

Our results and in-situ data suggest that ALT exhibits high spatial variability, perhaps reflecting local variability in topography or soil moisture. Since soil moisture reflects in part local topographic variation, measuring ground elevation to high precision may be important to understanding this variability.

5.4 Relation of meteorological parameters and ALT

We investigated correlations between ALT and several meteorological parameters, including ADDT and precipitation in thaw seasons from 2002 to 2022. ADDT and precipitation data are from the Sagwon meteorological station. Figure-7a shows the

https://doi.org/10.5194/egusphere-2023-2605
Preprint. Discussion started: 21 December 2023

relation between ADDT and ALT. From Stefan's equation, we expect a positive correlation between ADDT and ALT. However, the correlation is statistically weak (R-squared = 0.42; Figure-7b) suggesting the influence of additional factors. Precipitation may influence ALT, e.g., by advecting heat downward to promote permafrost thaw, but there are additional factors to consider. For example, an increase in soil moisture leads to a rise in the thermal conductivity of soil, potentially increasing the depth of the active layer during thaw season. However, an increase in soil moisture also increases the total amount of heat required for thawing, promoting a shallower active layer. Clayton et al. (2021) showed that ALT has a positive correlation with volumetric water content (VWC) in the upper 12 cm of soil, a negative correlation with bulk VWC, and no statistically correlation with VWC in the upper 20 cm of soil. We also do not see a statistically significant correlation between ALT and precipitation, perhaps reflecting these opposing impacts (Figure-7c).

We also used simple regression analyses to relate ALT to several multi-parameter factors including ADDT, precipitation and accumulated degree days of freezing (ADDF) from the previous year. However, these did not improve the correlation. Perhaps other factors such as local elevation gradients (influencing local hydrology), vegetation type, or the previous year's snowfall need to be considered.

5.5 Limitations and Future Research

Four aspects of our model may limit its utility:

1. Decorrelation of InSAR phase is the main limitation of this technique. Accurate InSAR measurements require a high degree of coherence, a measure of the correlation in radar phase between the two SAR images. Decorrelation occurs due to temporal changes in surface scattering properties, changes in viewing angles, and noise in the SAR data (Schaefer et al., 2015). C-band InSAR has demonstrated its ability to monitor deformation over continuous permafrost region at higher latitudes (see Previous Work). Wang et al. (2020) compared the efficiency of Sentinel-1 for monitoring permafrost deformation in discontinuous permafrost regions. They concluded that Sentinel-1 InSAR time-series performs effectively over discontinuous permafrost landscapes mainly beyond the tree line, such as tundra, tundra wetlands, and less developed shrub-tundra areas, during thaw season. However, the outcomes and precision are less favorable in shrub-tundra and forest-tundra environments. We compared temporal and spatial coherence between our study area and a discontinuous permafrost region near Fairbanks, Alaska, and obtained similar results. Decorrelation occurred around Beta site of the APEX ($\sim$30 km southwest of Fairbanks, Alaska) during the 2023 thaw season (Figure-S2). Land cover here is open black spruce forest. In contrast, temporal and spatial coherence remained high at CALM site U8 site, located in the continuous permafrost region to the north. Land cover here is classified as graminoid-moss tundra and graminoid, postrate-dwarf-shrub and moss tundra (See Study Area). Longer wavelengths such as L-band may be more useful in densely vegetated terrains. The launch of the NiSAR mission in 2024, with its L-band wavelength and repeat frequency of 6- 12 days, should prove useful for densely vegetated permafrost regions.

2. The spatial and temporal resolution of models that allow estimation of key ancillary parameters may limit accuracy in some regions, especially soil parameters from the GLDAS model, and atmospheric parameters from ERA-5. The spatial resolution of GLDAS' soil parameter model is 0.25 degree, an area that spans our entire study area in the Alaska north slope. The temporal resolution of ERA-5 is adequate, but its spatial resolution precludes local analysis.

https://doi.org/10.5194/egusphere-2023-2605
Preprint. Discussion started: 21 December 2023

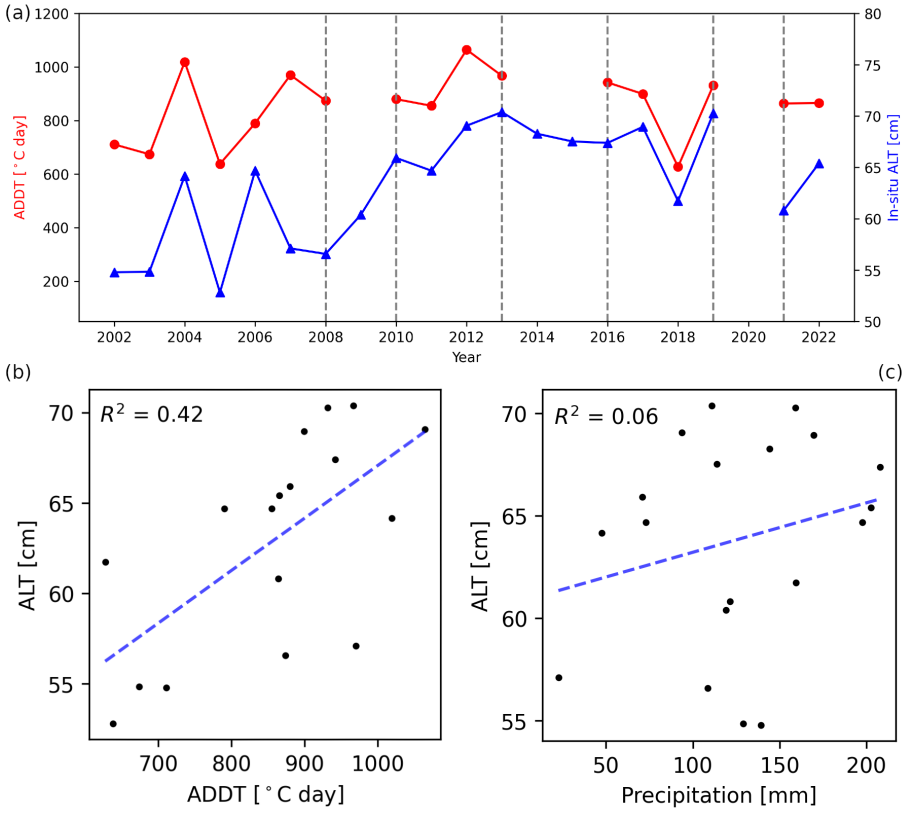

Figure 7. (a): Relation between ADDT and ALT from 2002 to 2022 in CALM site U8 and Sagwon station. Red circles show ADDT. Blue triangles show in-situ ALT. (b) scatter plot of ALT vs ADDT. (c) scatter plot of ALT vs precipitation. R-squared of relation is shown in top-left of panels. ADDT and precipitation are calculated from first of June to first of September of each year to be consistent with ALT measurements.

3. The model does not estimate long-term subsidence due to thawing of segregated ice, instead estimating ALT only by considering volume change from pore ice to water in the active layer. Development of a long-term (multi-year) ALT-subsidence model is desirable.

4. Accurate and dense porosity-depth and water content profiles based on in-situ data would also improve ALT estimation.

6 Conclusions

We used Sentinel-1 SAR data in the CALM site of northern Alaska for thaw season 2017 to 2022 to estimate active layer thickness using interferometric analysis. ALT estimates range from ∼20 cm to larger than 150 cm in our study area, similar to in-situ and previous remotely sensed estimates. ALT shows high spatial variability, sometimes changing dramatically between adjoining cells. Subsidence rate also varies between close points, ranging from ∼3-20 cm/year during the thaw season at our

https://doi.org/10.5194/egusphere-2023-2605
Preprint. Discussion started: 21 December 2023

study locations. Applying atmospheric corrections to C-band radar images improves signal to noise ratio. Limited ICESat-2 LiDAR data is consistent with the InSAR estimates of seasonal subsidence. Our results suggest that InSAR could be used to assess long-term continuous permafrost changes in the region.

Code and data availability.

Meteorological data from NOAA climate data online tool (CDO) is publicly available at (https://www.ncei.noaa.gov/cdo-web). Copernicus GLO-30 Digital Elevation Model is publicly available through (https://portal.opentopography.org). Sentinel-1 data are publicly available through Alaska Satellite Facility (https://search.asf.alaska.edu/#/). Interferograms were formed using Alaska Satellite Facility's Hybrid Pluggable Processing Pipeline (https://hyp3-docs.asf.alaska.edu/using/vertex/). Time-series analysis is done by using (https://github.com/insarlab/MintPy) in OpenScienceLab JupyterHub computing environment (https://opensciencelab.asf.alaska.edu). ERA-5 data for tropospheric corrections are available at (https://cds.climate.copernicus.eu). Soil fraction data are available at (https://ldas.gsfc.nasa.gov/gldas/soils). The code for ALT estimation is archived at (Sadeghi Chorsi, 2023).

Author contributions.

TSC, FJM, and THD conceptualized the overall study. TSC performed the data processing and analysis. TSC, FJM, and THD wrote and edited the manuscript. THD provided financial support for the study.

Competing interests.

The contact author has declared that none of the authors has any competing interests.

Acknowledgements. This project was funded by the NASA Earth Science program, grant 80NSSC22K1106 to THD. We thank anonymous reviewers for their valuable comments.

https://doi.org/10.5194/egusphere-2023-2605
Preprint. Discussion started: 21 December 2023

References

European Space Agency, Sinergise, https://doi.org/10.5069/G9028PQB, 2021.

Bakian-Dogaheh, K., Chen, R. H., Yi, Y., Kimball, J. S., Moghaddam, M., and Tabatabaeenejad, A.: A model to characterize soil moisture and organic matter profiles in the permafrost active layer in support of radar remote sensing in Alaskan Arctic tundra, Environmental Research Letters, 17, 025 011, 2022.

Bartsch, A., Leibman, M., Strozzi, T., Khomutov, A., Widhalm, B., Babkina, E., Mullanurov, D., Ermokhina, K., Kroisleitner, C., and Bergstedt, H.: Seasonal progression of ground displacement identified with satellite radar interferometry and the impact of unusually warm conditions on permafrost at the Yamal Peninsula in 2016, Remote Sensing, 11, 1865, https://doi.org/10.3390/rs11161865, 2019.

Bekaert, D., Hamlington, B., Buzzanga, B., and Jones, C.: Spaceborne synthetic aperture radar survey of subsidence in Hampton Roads, Virginia (USA), Scientific reports, 7, 14 752, https://doi.org/10.1038/s41598-017-15309-5, 2017.

Bürgmann, R., Rosen, P. A., and Fielding, E. J.: Synthetic aperture radar interferometry to measure Earth's surface topography and its deformation, Annual review of earth and planetary sciences, 28, 169–209, https://doi.org/10.1146/annurev.earth.28.1.169, 2000.

Castellazzi, P., Martel, R., Galloway, D. L., Longuevergne, L., and Rivera, A.: Assessing groundwater depletion and dynamics using GRACE and InSAR: Potential and limitations, Groundwater, 54, 768–780, https://doi.org/10.1111/gwat.12453, 2016.

CAVM Team, C. A. V. M.: Circumpolar Arctic vegetation map, (No Title), 2003.

Chen, C. W. and Zebker, H. A.: Phase unwrapping for large SAR interferograms: Statistical segmentation and generalized network models, IEEE Transactions on Geoscience and Remote Sensing, 40, 1709–1719, https://doi.org/10.1109/TGRS.2002.802453, 2002.

Chen, J., Günther, F., Grosse, G., Liu, L., and Lin, H.: Sentinel-1 InSAR measurements of elevation changes over Yedoma uplands on Sobo-Sise island, Lena Delta, Remote Sensing, 10, 1152, https://doi.org/10.3390/rs10071152, 2018.

Chen, J., Wu, Y., O'Connor, M., Cardenas, M. B., Schaefer, K., Michaelides, R., and Kling, G.: Active layer freeze-thaw and water storage dynamics in permafrost environments inferred from InSAR, Remote Sensing of Environment, 248, 112 007, https://doi.org/10.1016/j.rse.2020.112007, 2020.

Chen, R., Michaelides, R., Chen, J., Chen, A., Clayton, L., Bakian-Dogaheh, K., Huang, L., Jafarov, E., Liu, L., Moghaddam, M., et al.: ABoVE: Active Layer Thickness from Airborne L-and P-band SAR, Alaska, 2017, Ver. 3, ORNL DAAC, https://doi.org/10.3334/ORNLDAAC/2004, 2022.

Chen, R. H., Michaelides, R. J., Zhao, Y., Huang, L., Wig, E., Sullivan, T. D., Parsekian, A. D., Zebker, H. A., Moghaddam, M., and Schaefer, K. M.: Permafrost Dynamics Observatory (PDO): 2. Joint Retrieval of Permafrost Active Layer Thickness and Soil Moisture From L-Band InSAR and P-Band PolSAR, Earth and Space Science, 10, e2022EA002 453, https://doi.org/10.1029/2020EA001630, 2023.

Clayton, L. K., Schaefer, K., Battaglia, M. J., Bourgeau-Chavez, L., Chen, J., Chen, R. H., Chen, A., Bakian-Dogaheh, K., Grelik, S., Jafarov, E., et al.: Active layer thickness as a function of soil water content, Environmental Research Letters, 16, 055 028, https://doi.org/10.1088/1748-9326/abfa4c, 2021.

Dammann, D. O., Eriksson, L. E., Mahoney, A. R., Eicken, H., and Meyer, F. J.: Mapping pan-Arctic landfast sea ice stability using Sentinel-1 interferometry, The Cryosphere, 13, 557–577, https://doi.org/10.5194/tc-13-557-2019, 2019.

Daout, S., Doin, M.-P., Peltzer, G., Socquet, A., and Lasserre, C.: Large-scale InSAR monitoring of permafrost freeze-thaw cycles on the Tibetan Plateau, Geophysical Research Letters, 44, 901–909, https://doi.org/10.1002/2016GL070781, 2017.

Deng, F., Dixon, T. H., and Xie, S.: Surface deformation and induced seismicity due to fluid injection and oil and gas extraction in western Texas, Journal of Geophysical Research: Solid Earth, 125, e2019JB018 962, https://doi.org/10.1029/2019JB018962, 2020.

https://doi.org/10.5194/egusphere-2023-2605
Preprint. Discussion started: 21 December 2023

Ding, X.-l., Li, Z.-w., Zhu, J.-j., Feng, G.-c., and Long, J.-p.: Atmospheric effects on InSAR measurements and their mitigation, Sensors, 8, 5426–5448, https://doi.org/10.3390/s8095426, 2008.

Dobinski, W.: Permafrost, Earth-Science Reviews, 108, 158–169, https://doi.org/10.1016/j.earscirev.2011.06.007, 2011.

Doin, M.-P., Lasserre, C., Peltzer, G., Cavalié, O., and Doubre, C.: Corrections of stratified tropospheric delays in SAR interferometry: Validation with global atmospheric models, Journal of Applied Geophysics, 69, 35–50, https://doi.org/10.1016/j.jappgeo.2009.03.010, 2009.

Fattahi, H., Agram, P., and Simons, M.: A network-based enhanced spectral diversity approach for TOPS time-series analysis, IEEE Transactions on Geoscience and Remote Sensing, 55, 777–786, https://doi.org/10.1109/TGRS.2016.2614925, 2016.

Goldstein, R. M. and Werner, C. L.: Radar interferogram filtering for geophysical applications, Geophysical research letters, 25, 4035–4038, https://doi.org/10.1029/1998GL900033, 1998.

Grapenthin, R., Cheng, Y., Angarita, M., Tan, D., Meyer, F. J., Fee, D., and Wech, A.: Return from Dormancy: Rapid inflation and seismic unrest driven by transcrustal magma transfer at Mt. Edgecumbe (L'úx Shaa) Volcano, Alaska, Geophysical Research Letters, 49, e2022GL099 464, https://doi.org/10.1029/2022GL099464, 2022.

Grigal, D., Brovold, S., Nord, W., and Ohmann, L.: Bulk density of surface soils and peat in the north central United States, Canadian Journal of Soil Science, 69, 895–900, https://doi.org/10.4141/cjss89-092, 1989.

Hanssen, R. F.: Radar interferometry: data interpretation and error analysis, vol. 2, Springer Science & Business Media, 2001.

Hersbach, H., Bell, B., Berrisford, P., Hirahara, S., Horányi, A., Muñoz-Sabater, J., Nicolas, J., Peubey, C., Radu, R., Schepers, D., et al.: The ERA5 global reanalysis, Quarterly Journal of the Royal Meteorological Society, 146, 1999–2049, https://doi.org/10.1002/qj.3803, 2020.

Hogenson, K., Kristenson, H., Kennedy, J., Johnston, A., Rine, J., Logan, T., Zhu, J., Williams, F., Herrmann, J., Smale, J., and Meyer, F.: Hybrid Pluggable Processing Pipeline (HyP3): A cloud-native infrastructure for generic processing of SAR data [Computer software], https://doi.org/10.5281/zenodo.4646138, 2020.

Honglei, Y., Qiao, J., Jianfeng, H., Ki-Yeob, K., and Junhuan, P.: InSAR measurements of surface deformation over permafrost on Fenghuoshan Mountains section, Qinghai-Tibet Plateau, Journal of Systems Engineering and Electronics, 32, 1284–1303, https://doi.org/10.23919/JSEE.2021.000109, 2021.

Hossain, M., Chen, W., and Zhang, Y.: Bulk density of mineral and organic soils in the Canada's arctic and sub-arctic, Information processing in agriculture, 2, 183–190, https://doi.org/10.1016/j.inpa.2015.09.001, 2015.

Hu, Y., Liu, L., Larson, K. M., Schaefer, K. M., Zhang, J., and Yao, Y.: GPS interferometric reflectometry reveals cyclic elevation changes in thaw and freezing seasons in a permafrost area (Barrow, Alaska), Geophysical Research Letters, 45, 5581–5589, https://doi.org/10.1029/2018GL077960, 2018.

Iwahana, G., Uchida, M., Liu, L., Gong, W., Meyer, F. J., Guritz, R., Yamanokuchi, T., and Hinzman, L.: InSAR detection and field evidence for thermokarst after a tundra wildfire, using ALOS-PALSAR, Remote Sensing, 8, 218, https://doi.org/10.3390/rs8030218, 2016.

Jackson, R., Mooney, H., and Schulze, E.-D.: Global distribution of fine root biomass in terrestrial ecosystems, ORNL DAAC, https://doi.org/10.3334/ORNLDAAC/658, 2003.

Johnson, K. D., Harden, J., McGuire, A. D., Bliss, N. B., Bockheim, J. G., Clark, M., Nettleton-Hollingsworth, T., Jorgenson, M. T., Kane, E. S., Mack, M., et al.: Soil carbon distribution in Alaska in relation to soil-forming factors, Geoderma, 167, 71–84, https://doi.org/10.1016/j.geoderma.2011.10.006, 2011.

Jolivet, R., Grandin, R., Lasserre, C., Doin, M.-P., and Peltzer, G.: Systematic InSAR tropospheric phase delay corrections from global meteorological reanalysis data, Geophysical Research Letters, 38, https://doi.org/10.1029/2011GL048757, 2011.

https://doi.org/10.5194/egusphere-2023-2605
Preprint. Discussion started: 21 December 2023

Jolivet, R., Agram, P. S., Lin, N. Y., Simons, M., Doin, M.-P., Peltzer, G., and Li, Z.: Improving InSAR geodesy using global atmospheric models, Journal of Geophysical Research: Solid Earth, 119, 2324–2341, https://doi.org/10.1002/2013JB010588, 2014.

Jorgenson, M., Yoshikawa, K., Kanevskiy, M., Shur, Y., Romanovsky, V., Marchenko, S., Grosse, G., Brown, J., and Jones, B.: Permafrost characteristics of Alaska, in: Proceedings of the ninth international conference on permafrost, vol. 3, pp. 121–122, University of Alaska Fairbanks, 2008.

Liu, L. and Larson, K. M.: Decadal changes of surface elevation over permafrost area estimated using reflected GPS signals, The Cryosphere, 12, 477–489, https://doi.org/10.5194/tc-12-477-2018, 2018.

Liu, L., Zhang, T., and Wahr, J.: InSAR measurements of surface deformation over permafrost on the North Slope of Alaska, Journal of Geophysical Research: Earth Surface, 115, https://doi.org/10.1029/2009JF001547, 2010.

Liu, L., Schaefer, K., Zhang, T., and Wahr, J.: Estimating 1992–2000 average active layer thickness on the Alaskan North Slope from remotely sensed surface subsidence, Journal of Geophysical Research: Earth Surface, 117, https://doi.org/10.1029/2011JF002041, 2012.

Liu, L., Jafarov, E. E., Schaefer, K. M., Jones, B. M., Zebker, H. A., Williams, C. A., Rogan, J., and Zhang, T.: InSAR detects increase in surface subsidence caused by an Arctic tundra fire, Geophysical Research Letters, 41, 3906–3913, https://doi.org/10.1002/2014GL060533, 2014.

Liu, L., Schaefer, K., Chen, A., Gusmeroli, A., Zebker, H., and Zhang, T.: Remote sensing measurements of thermokarst subsidence using InSAR, Journal of Geophysical Research: Earth Surface, 120, 1935–1948, https://doi.org/10.1002/2015JF003599, 2015.

Meyer, F., Kampes, B., Bamler, R., and Fischer, J.: Methods for atmospheric correction in InSAR data, in: Fringe 2005 Workshop, vol. 610, 2006.

Meyer, F. J.: Performance requirements for ionospheric correction of low-frequency SAR data, IEEE transactions on geoscience and remote sensing, 49, 3694–3702, https://doi.org/10.1109/TGRS.2011.2146786, 2011.

Michaelides, R. J., Schaefer, K., Zebker, H. A., Parsekian, A., Liu, L., Chen, J., Natali, S., Ludwig, S., and Schaefer, S. R.: Inference of the impact of wildfire on permafrost and active layer thickness in a discontinuous permafrost region using the remotely sensed active layer thickness (ReSALT) algorithm, Environmental Research Letters, 14, 035 007, https://doi.org/10.1088/1748-9326/aaf932, 2019.

Michaelides, R. J., Chen, R. H., Zhao, Y., Schaefer, K., Parsekian, A. D., Sullivan, T., Moghaddam, M., Zebker, H. A., Liu, L., Xu, X., et al.: Permafrost Dynamics Observatory—Part I: Postprocessing and Calibration Methods of UAVSAR L-Band InSAR Data for Seasonal Subsidence Estimation, Earth and Space Science, 8, e2020EA001 630, https://doi.org/10.1029/2020EA001630, 2021.

Mishra, U. and Riley, W. J.: Alaskan soil carbon stocks: spatial variability and dependence on environmental factors, Biogeosciences, 9, 3637–3645, https://doi.org/10.5194/bg-9-3637-2012, 2012.

Nelson, F., Shiklomanov, N., Mueller, G., Hinkel, K., Walker, D., and Bockheim, J.: Estimating active-layer thickness over a large region: Kuparuk River basin, Alaska, USA, Arctic and Alpine Research, 29, 367–378, https://doi.org/10.1080/00040851.1997.12003258, 1997.

Neuenschwander, A. and Pitts, K.: The ATL08 land and vegetation product for the ICESat-2 Mission, Remote sensing of environment, 221, 247–259, https://doi.org/10.1016/j.rse.2018.11.005, 2019.

Neuenschwander, A. L. and Magruder, L. A.: Canopy and terrain height retrievals with ICESat-2: A first look, Remote sensing, 11, 1721, https://doi.org/10.3390/rs11141721, 2019.

Neuenschwander, A. L., Pitts, K., Jelley, B., Robbins, J., Klotz, B., Popescu, S. C., Nelson, R. F., Harding, D., Pederson, D., and Sheridan, R.: ATLAS/ICESat-2 L3A Land and Vegetation Height, Version 3, Boulder, Colorado USA. NASA National Snow and Ice Data Center Distributed Active Archive Center, https://doi.org/10.5067/ATLAS/ATL08.005, 2021.

https://doi.org/10.5194/egusphere-2023-2605
Preprint. Discussion started: 21 December 2023

Peddle, D. R. and Franklin, S. E.: Classification of permafrost active layer depth from remotely sensed and topographic evidence, Remote Sensing of Environment, 44, 67–80, https://doi.org/10.1016/0034-4257(93)90103-5, 1993.

Poland, M. P. and Zebker, H. A.: Volcano geodesy using InSAR in 2020: the past and next decades, Bulletin of Volcanology, 84, 27, https://doi.org/10.1007/s00445-022-01531-1, 2022.

Riseborough, D.: Thawing and freezing indices in the active layer, in: Proceedings of the 8th International Conference on Permafrost, vol. 2, pp. 953–958, Rotterdam: AA Balkema, 2003.

Rodell, M., Houser, P., Jambor, U., Gottschalck, J., Mitchell, K., Meng, C.-J., Arsenault, K., Cosgrove, B., Radakovich, J., Bosilovich, M., et al.: The global land data assimilation system, Bulletin of the American Meteorological society, 85, 381–394, https://doi.org/10.1175/BAMS-85-3-381, 2004.

Rykhus, R. P. and Lu, Z.: InSAR detects possible thaw settlement in the Alaskan Arctic Coastal Plain, Canadian Journal of Remote Sensing, 34, 100–112, https://doi.org/10.5589/m08-018, 2008.

Sadeghi Chorsi, T.: Activer Layer Thickness Estimation using InSAR, Meteorologiical data and Soil parameters, https://doi.org/10.5281/zenodo.10023340, 2023.

Sadeghi Chorsi, T., Braunmiller, J., Deng, F., and Dixon, T. H.: Afterslip from the 2020 M 6.5 Monte Cristo Range, Nevada Earthquake, Geophysical Research Letters, 49, e2022GL099 952, https://doi.org/10.1029/2022GL099952, 2022a.

Sadeghi Chorsi, T., Braunmiller, J., Deng, F., Mueller, N., Kerstetter, S., Stern, R. J., and Dixon, T. H.: The May 15, 2020 M 6.5 Monte Cristo Range, Nevada, earthquake: eyes in the sky, boots on the ground, and a chance for students to learn, International Geology Review, 64, 2683–2702, https://doi.org/10.1080/00206814.2021.2000507, 2022b.

Schaefer, K., Zhang, T., Slater, A. G., Lu, L., Etringer, A., and Baker, I.: Improving simulated soil temperatures and soil freeze/thaw at high-latitude regions in the Simple Biosphere/Carnegie-Ames-Stanford Approach model, Journal of Geophysical Research: Earth Surface, 114, https://doi.org/10.1029/2008JF001125, 2009.

Schaefer, K., Liu, L., Parsekian, A., Jafarov, E., Chen, A., Zhang, T., Gusmeroli, A., Panda, S., Zebker, H. A., and Schaefer, T.: Remotely sensed active layer thickness (ReSALT) at Barrow, Alaska using interferometric synthetic aperture radar, Remote sensing, 7, 3735–3759, https://doi.org/10.3390/rs70403735, 2015.

Singhroy, V., Alasset, P.-J., Couture, R., and Poncos, V.: InSAR monitoring of landslides on permafrost terrain in Canada, in: 2007 IEEE International Geoscience and Remote Sensing Symposium, pp. 2451–2454, IEEE, https://doi.org/10.1109/IGARSS.2007.4423338, 2007.

Strozzi, T., Antonova, S., Günther, F., Mätzler, E., Vieira, G., Wegmüller, U., Westermann, S., and Bartsch, A.: Sentinel-1 SAR interferometry for surface deformation monitoring in low-land permafrost areas, Remote Sensing, 10, 1360, https://doi.org/10.3390/rs10091360, 2018.

Vasco, D. W., Dixon, T. H., Ferretti, A., and Samsonov, S. V.: Monitoring the fate of injected CO2 using geodetic techniques, The Leading Edge, 39, 29–37, https://doi.org/10.1190/tle39010029.1, 2020.

Wang, L., Marzahn, P., Bernier, M., and Ludwig, R.: Sentinel-1 InSAR measurements of deformation over discontinuous permafrost terrain, Northern Quebec, Canada, Remote Sensing of Environment, 248, 111 965, https://doi.org/10.1016/j.rse.2020.111965, 2020.

Yang, Q., Zhao, W., Dixon, T. H., Amelung, F., Han, W. S., and Li, P.: InSAR monitoring of ground deformation due to CO2 injection at an enhanced oil recovery site, West Texas, International Journal of Greenhouse Gas Control, 41, 20–28, https://doi.org/10.1016/j.ijggc.2015.06.016, 2015.

Yunjun, Z., Fattahi, H., and Amelung, F.: Small baseline InSAR time series analysis: Unwrapping error correction and noise reduction, Computers & Geosciences, 133, 104 331, https://doi.org/10.1016/j.cageo.2019.104331, 2019.

https://doi.org/10.5194/egusphere-2023-2605
Preprint. Discussion started: 21 December 2023

Zhang, X., Jones, C. E., Oliver-Cabrera, T., Simard, M., and Fagherazzi, S.: Using rapid repeat SAR interferometry to improve hydrodynamic
450 models of flood propagation in coastal wetlands, Advances in Water Resources, 159, 104 088, https://doi.org/10.1016/j.advwatres.2021.
104088, 2022.